Exploring short range correlations through $\gamma n \to \pi^- p$ in the GlueX detector

J. R. Pybus, P. Sharp, and H. Szumila-Vance
for the SRC@GlueX Collaboration

1 Event Generators

This study modelled separately ^{4}He$(\gamma, \pi^- p)$ events resulting from neutrons from short range-correlated (SRC) pairs and those from mean-field neutrons (See Fig. 2). We generated Monte Carlo samples of signal events for both the mean-field and SRC in the beam energy range between 8.4 GeV and 9.1 GeV according to the spectrum shown in Fig. 1. The photon beam spectrum was taken from one of the GlueX production runs on the diamond radiator. The position of the coherent peak corresponds to about 9.1 GeV. The cross section for $\gamma n \to \pi^- p$ was parameterized by the form [1]:

$$\frac{d\sigma^{\gamma n}}{dt} = As^{-b}(1-\cos\theta^*)^{-c}(1+\cos\theta^*)^{-d} \tag{1}$$

where A, b, c, d were fit to measurements of the $\gamma p \to \pi^+ n$ cross section, which is related by isospin symmetry. Reactions with mean-field neutrons were modelled using the mean-field spectral function. SRC reactions were modelled using the Generalized Contact Formalism [2–6]. Distributions for the final-state particles in generated SRC events with $s, |t|, |u| > 2$ GeV^2 are shown in Fig. 3.

2 Simulation in the GlueX detector

Generated events were passed through the detailed GlueX detector simulation (Geant 3.21 and mcsmear). For the analysis, we used the official Hall D reconstruction software (halld_recon). The level 1 trigger was simulated by requiring the total energy deposition in the FCAL and BCAL to

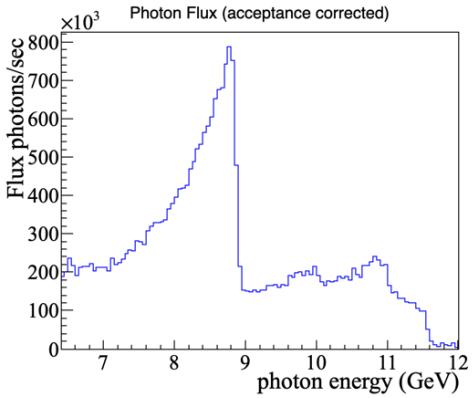

Figure 1: The photon energy spectrum in GlueX.

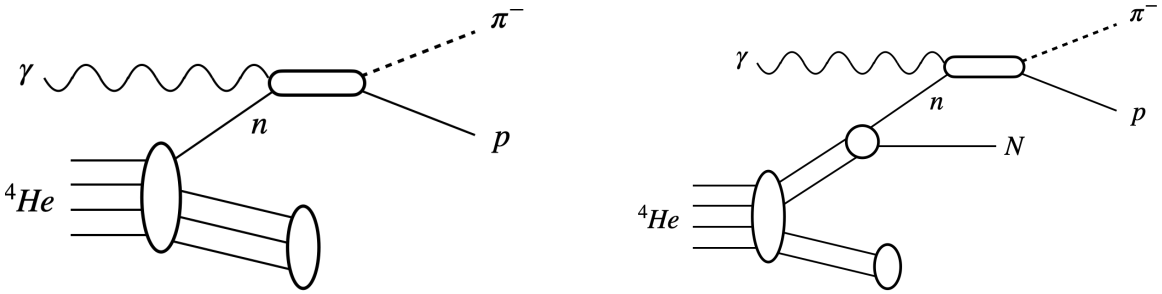

Figure 2: The PWIA diagrams used to calculate event cross sections are shown, including both mean-field reactions (left) and SRC reactions (right).

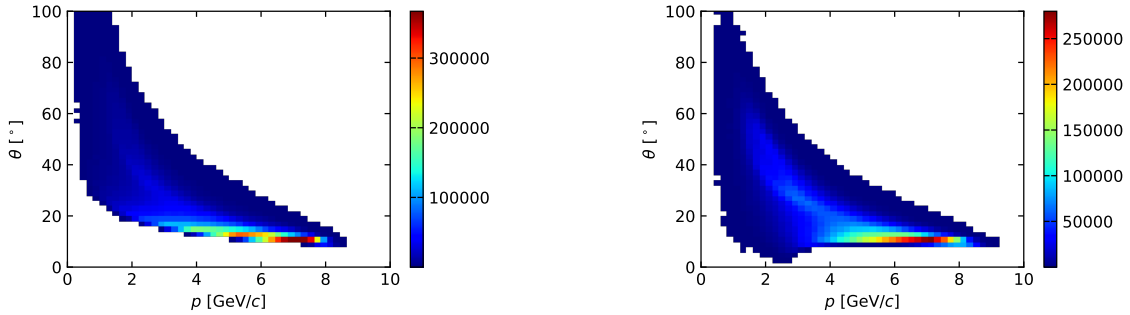

Figure 3: Generated distributions for pion (left) and proton (right) kinematics in SRC photoproduction events with $s, |t|, |u| > 2$ GeV^2.

satisfy the following equation:

$$0.7 \times E_{FCAL} + E_{BCAL} > 180\text{MeV} \tag{2}$$

where E_{FCAL} and E_{BCAL} are the energy deposition in the forward and barrel calorimeters, respectively, for a given event. Events also triggered a hit in the start counter. This is the tested and proposed trigger configuration for the SRC experiment to run in Hall D. For the generated events, the trigger efficiency for detected events was found to be 100%.

The reconstructed energy of the beam photon was taken from the DBeamPhoton factory. Charged tracks were reconstructed in the central and forward drift chambers. For the large particle momentum, no particle identification was performed. Track fitting procedure enabled the discrimination of positive and negative particles. The negative and positive track candidates were assigned to the π^- and proton, respectively.

2.1 Reconstruction Resolutions

Fig. 4 shows the momentum resolution for π^- and p as a function of polar angle. We see that the simulated resolutions are comparable to those measured in Ref. [7]. We note that the highest-momentum events occur at very forward angles, resulting in an increased path length which compensates for the effects of increased momentum.

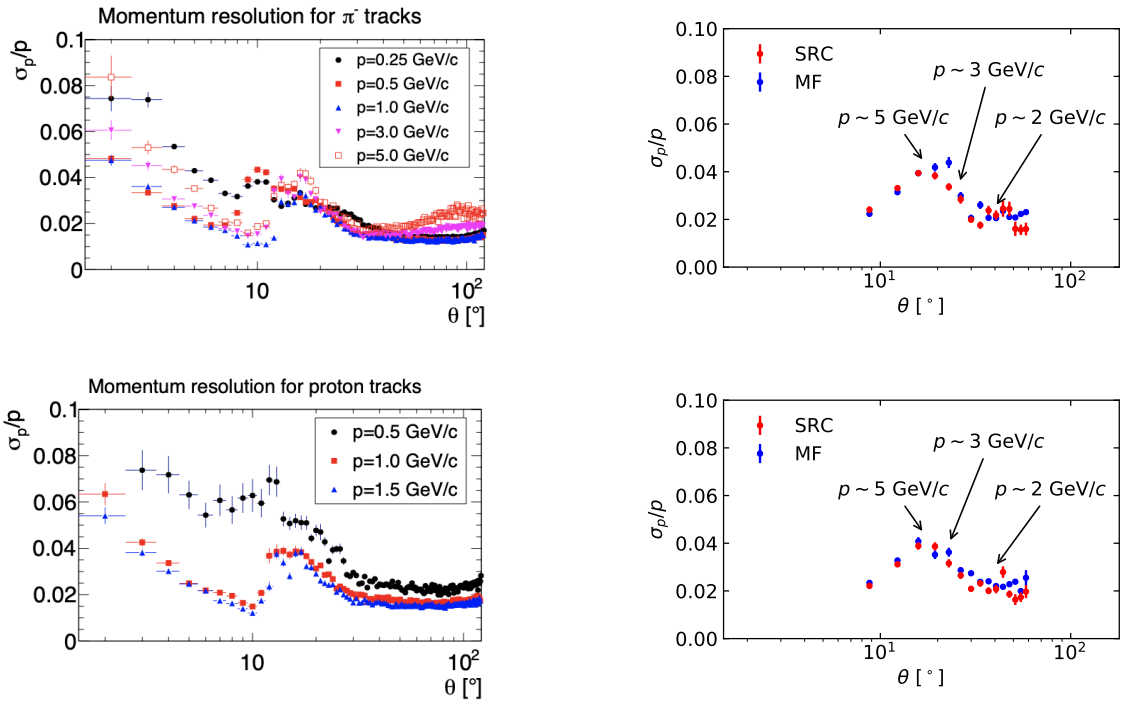

Figure 4: Comparison between π^- (top) and proton (bottom) momentum resolution in Ref. [7] (left) and this study (right).

3 Optimization of event selection

Separation between mean-field and SRC nucleons usually relies on reconstruction of the missing momentum $p_{miss} = (\epsilon_{miss}, \mathbf{p_{miss}}) \equiv p_p + p_\pi - p_\gamma \approx p_i$, which allows event discrimination based on the initial state of the struck neutron. The SRC-dominated region is typically taken to be $|\mathbf{p_{miss}}| > 300$ MeV/c, sufficiently above the Fermi momentum such that the mean-field contribution is negligible. Fig. 5 shows the separation between the mean-field and SRC regions in both $|\mathbf{p_{miss}}|$ and ϵ_{miss} in event generation for accepted events, as well as the effect of bin migration on these quantities. As can be seen, the low resolution of GlueX results in bin migration but still allows distinguishing SRC events from mean-field background.

Furthermore, we may mitigate these resolution effects using light front kinematics. By defining $p^- \equiv p^0 - p^3$ and $\mathbf{p}_\perp \equiv (p^1, p^2)$, with the 3-direction defined along the beam direction, we may examine the effects of bin migration on these components of the missing momentum, shown in Fig. 6, and note that both are sufficiently well-reconstructed to separate SRC and mean-field events.

This improved separation results from a cancellation of the effects of resolution in the difference of the reconstructed energy and momentum. We may examine the explicit formula for p^-_{miss}:

$$p^-_{miss} \equiv \epsilon_{miss} - p^3_{miss} = \sqrt{p_p^2 + m_p^2} + \sqrt{p_\pi^2 + m_\pi^2} - p_p^3 - p_\pi^3 \tag{3}$$

where the energy and momentum of the photon cancel due to our choice of coordinate system. If we examine the uncertainty on this quantity resulting from the uncertainty in the magnitudes of

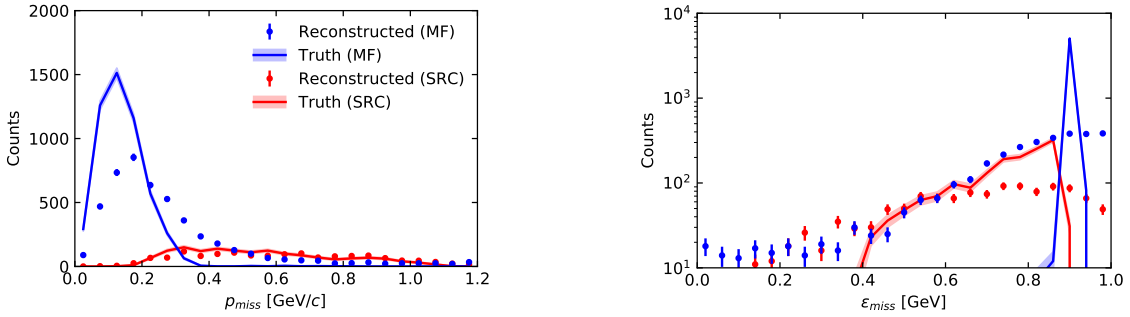

Figure 5: Distributions of $|\mathbf{p_{miss}}|$ (left) and ϵ_{miss} (right) for mean-field (blue) and SRC (red) events, including the effects of bin migration.

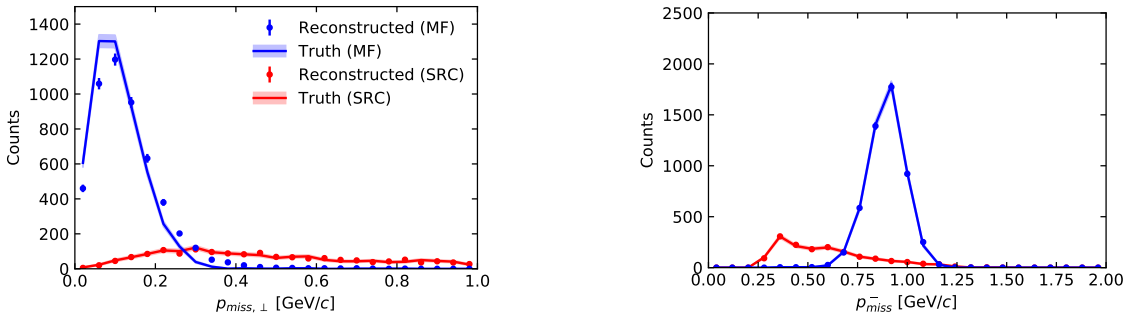

Figure 6: Distributions of $|\mathbf{p_{miss,\perp}}|$ (left) and p^-_{miss} (right) for mean-field (blue) and SRC (red) events, including the effects of bin migration.

momenta of the final-state particles:

$$\begin{aligned}\left(\delta p^-_{miss}\right)^2 &= \left(\frac{p_p}{\sqrt{p_p^2+m_p^2}}-\cos\theta_p\right)^2\left(\delta p_p\right)^2+\left(\frac{p_\pi}{\sqrt{p_\pi^2+m_\pi^2}}-\cos\theta_\pi\right)^2\left(\delta p_\pi\right)^2 \\ &= \left(\beta_p-\cos\theta_p\right)^2\left(\delta p_p\right)^2+\left(\beta_\pi-\cos\theta_\pi\right)^2\left(\delta p_\pi\right)^2\end{aligned} \tag{4}$$

we note some cancellation in both terms, which takes the difference of two positive quantities. We have neglected resolution on θ, as angular resolution is much better than momentum resolution for these particle; see Figs 13 and 14 in the Appendix. This is exacerbated by the kinematics of the reaction, shown in Fig. 3, which shows that those highest momentum particles, with larger β, are also further forward and therefore have an increased $\cos\theta$. This method of performing analysis on the light front has similarly been used to mitigate resolution effects in $(p,2p)$ studies of SRCs [8–11].

We may define a quantity:

$$k^2_{miss} \equiv m_N^2\left(\frac{p^2_{miss,\perp}+m_N^2}{p^-_{miss}(2m_N-p^-_{miss})}\right)-m_N^2 \tag{5}$$

which is equivalent to an SRC internal momentum, as defined in Ref. [12], assuming breakup of a standing SRC pair. Fig. 7 shows contours of constant k_{miss} on the p^-_{miss}-$|\mathbf{p_{miss,\perp}}|$ plane for reconstructed events, demonstrating that this observable captures the separation between the mean-field and SRC events.

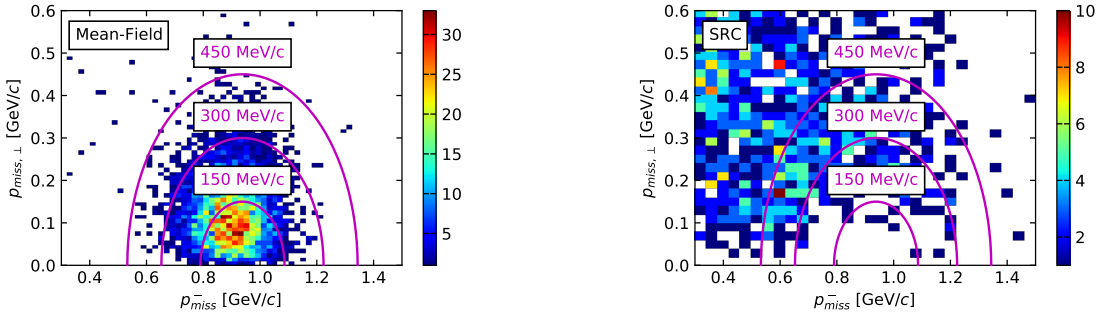

Figure 7: Distributions of p_{miss}^{-} and $|\mathbf{p_{miss,\perp}}|$ for reconstructed mean-field (left) and SRC (right) events, with contours of constant k_{miss} in magenta.

Fig. 8 shows the purity (fraction of events which are from SRC breakup) and the efficiency (fraction of SRC events captured within the cut) of the signal captured within a given k_{miss} cut. We can see that requiring $k_{miss} > 350$ MeV/c results in a signal with 80% SRC purity, while capturing 90% of generated SRC events. As such, we can clearly distinguish the SRC signal from the mean-field background.

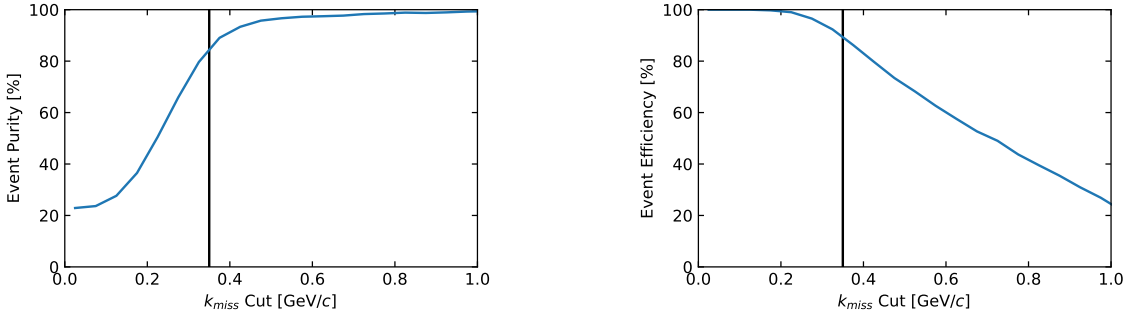

Figure 8: SRC event purity (left) and efficiency (right) as a function of lower cut on k_{miss}. A cut at $k_{miss} = 350$ MeV/c is demonstrated in both figures.

Fig. 9 shows the fraction of ^{4}He$(\gamma, \pi^- p)$ events resulting in a detected recoil particle as a function of both p_{miss} and k_{miss}; this is the first target observable for this study, which would provide an independent observation of the tensor-to-scalar transition in the NN interaction, previously observed in Refs. [5, 13]. We note that while bin-migration effects largely cancel in the ratio, the choice of k_{miss} as the observable again mitigates these effects. Table 1 in the Appendix shows the estimated bin-migration for SRC events as a function of both p_{miss} and k_{miss}, demonstrating the advantages of using k_{miss} as the observable of choice.

4 Summary

We have demonstrated that the GlueX detector is capable of measuring SRC breakup photoproduction events to satisfactory precision and that isolation of SRC events from mean-field background may be ensured by performing cuts and analysis on the light-front.

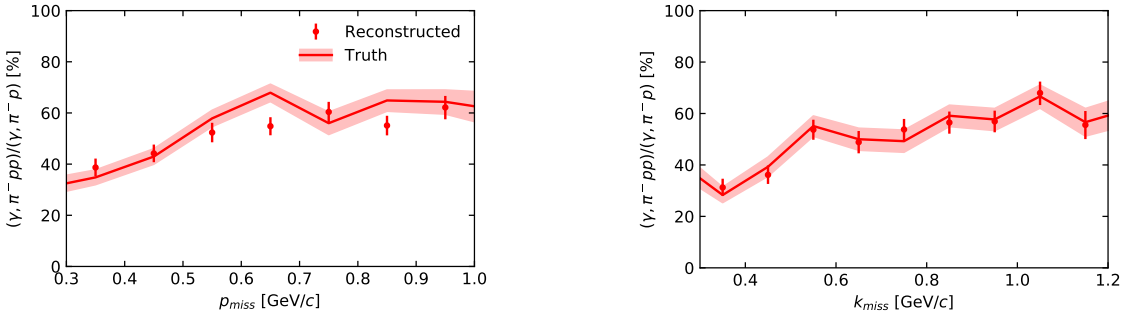

Figure 9: Recoil proton tagging fraction as a function of p_{miss} (left) and k_{miss} (right), including the effects of bin migration.

References

[1] R. L. Anderson, D. B. Gustavson, D. M. Ritson, G. A. Weitsch, H. J. Halpern, R. Prepost, D. H. Tompkins, and D. E. Wiser, "Measurements of exclusive photoproduction processes at large values of t and u from 4 to 7.5 gev," *Phys. Rev. D*, vol. 14, pp. 679–697, Aug 1976.

[2] R. Cruz-Torres, D. Lonardoni, R. Weiss, N. Barnea, D. W. Higinbotham, E. Piasetzky, A. Schmidt, L. B. Weinstein, R. B. Wiringa, and O. Hen, "Scale and scheme independence and position-momentum equivalence of nuclear short-range correlations," 2019.

[3] R. Weiss, B. Bazak, and N. Barnea, "Generalized nuclear contacts and momentum distributions," *Physical Review C*, vol. 92, Nov 2015.

[4] R. Weiss, R. Cruz-Torres, N. Barnea, E. Piasetzky, and O. Hen, "The nuclear contacts and short range correlations in nuclei," *Physics Letters B*, vol. 780, pp. 211 – 215, 2018.

[5] A. Schmidt, J. Pybus, R. Weiss, E. Segarra, A. Hrnjic, A. Denniston, O. Hen, E. Piasetzky, L. Weinstein, N. Barnea, M. Strikman, A. Larionov, and D. Higinbotham, "Probing the core of the strong nuclear interaction," *Nature*, vol. 578, pp. 540–544, 02 2020.

[6] J. Pybus, I. Korover, R. Weiss, A. Schmidt, N. Barnea, D. Higinbotham, E. Piasetzky, M. Strikman, L. Weinstein, and O. Hen, "Generalized contact formalism analysis of the 4he(e,e'pn) reaction," *Physics Letters B*, vol. 805, p. 135429, Jun 2020.

[7] S. Adhikari *et al.*, "The GlueX Beamline and Detector," 5 2020.

[8] Y. Mardor, J. Aclander, J. Alster, D. Barton, G. Bunce, A. Carroll, N. Christensen, H. Courant, S. Durrant, S. Gushue, and et al., "Measurement of quasi-elastic c(p,2p) scattering at high momentum transfer," *Physics Letters B*, vol. 437, p. 257–263, Oct 1998.

[9] I. Yaron, L. Frankfurt, E. Piasetzky, M. Sargsian, and M. Strikman, "Investigation of the high momentum components of the nuclear wave function using hard quasielastica(p,2p)xreactions," *Physical Review C*, vol. 66, Aug 2002.

[10] A. Tang, J. W. Watson, J. Aclander, J. Alster, G. Asryan, Y. Averichev, D. Barton, V. Baturin, N. Bukhtoyarova, A. Carroll, and et al., "n-p short-range correlations from (p,2p+n) measurements," *Physical Review Letters*, vol. 90, Jan 2003.

[11] E. Piasetzky, M. Sargsian, L. Frankfurt, M. Strikman, and J. W. Watson, "Evidence for strong dominance of proton-neutron correlations in nuclei," *Physical Review Letters*, vol. 97, Oct 2006.

[12] L. L. Frankfurt and M. I. Strikman, "High-energy phenomena, short-range nuclear structure and qcd," *Phys. Rep.*, vol. 76, no. 4, p. 215, 1981.

[13] I. Korover, J. R. Pybus, A. Schmidt, F. Hauenstein, M. Duer, O. Hen, E. Piasetzky, L. B. Weinstein, D. W. Higinbotham, and the CLAS Collaboration, "Tensor-to-scalar transition in the nucleon-nucleon interaction mapped by ^{12}c(e,e′pn) measurements," 2020.

5 Appendix

Bin Range	p_{miss} Bin Migration	k_{miss} Bin Migration
300-400 MeV/c	-26.3%	-12.3%
400-500 MeV/c	-30.6%	+5.4%
500-600 MeV/c	-27.7%	+3.8%
600-700 MeV/c	+5.3%	-2.2%
700-800 MeV/c	+19.2%	+9.8%
800-900 MeV/c	+27.5%	-4.4%
900-1000 MeV/c	+9.9%	+5.4%
1000-1100 MeV/c	+73.9%	-4.6%
1100-1200 MeV/c	+1750.0%	-2.4%

Table 1: Estimated bin-migration for 100 MeV/c bins in p_{miss} and k_{miss}.

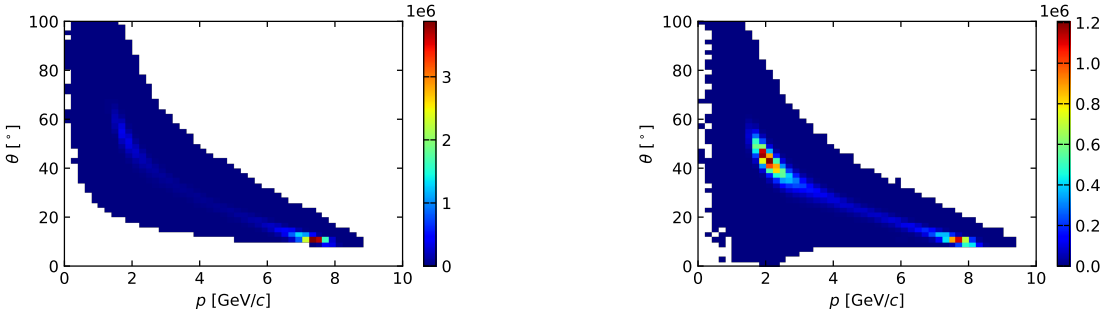

Figure 10: Generated distributions for pion (left) and proton (right) kinematics in Mean-Field photoproduction events with $s, |t|, |u| > 2$ GeV^2.

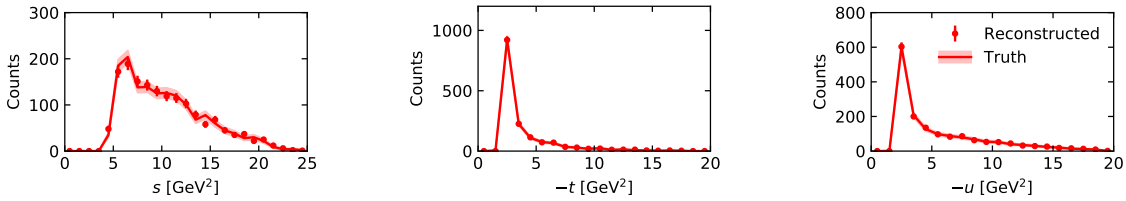

Figure 11: Distributions of s (left), t (center), and u (right) for SRC events, including the effects of bin migration.

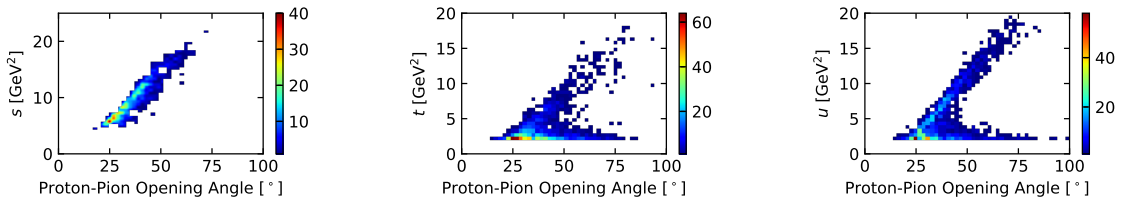

Figure 12: Pion-proton opening angle compared to s (left), t (center), and u (right) for reconstructed SRC events.

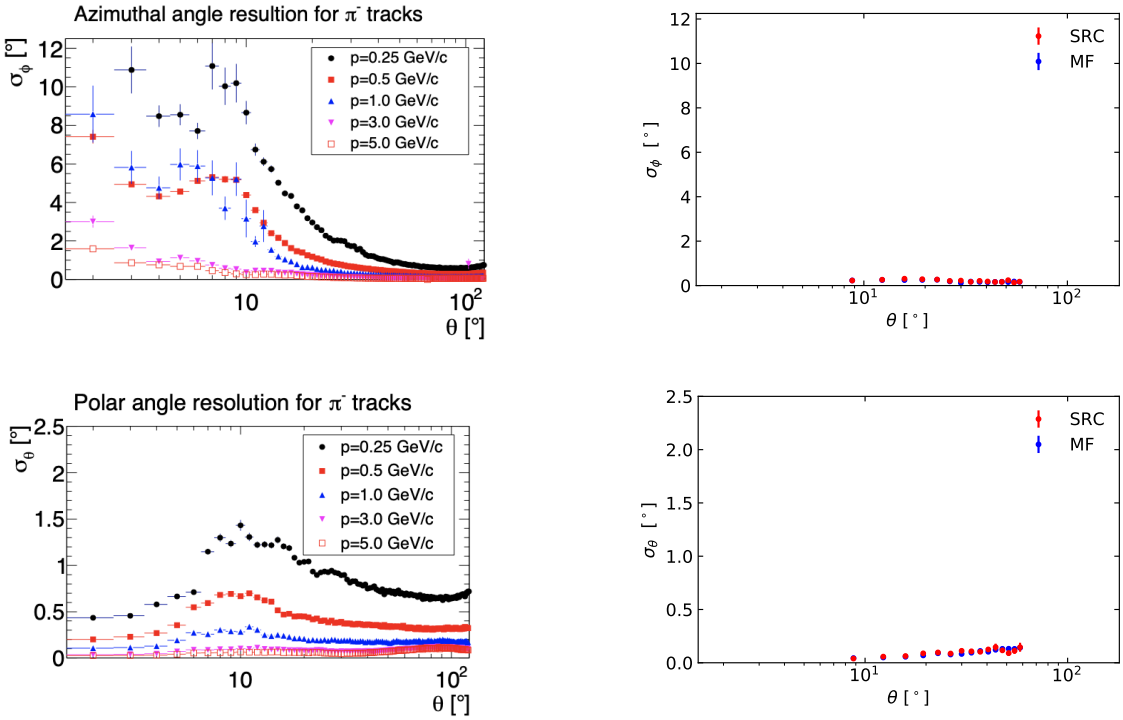

Figure 13: Comparison between π^- angular resolutions for ϕ (top) and θ (bottom) resolution in Ref. [7] (left) and this study (right)

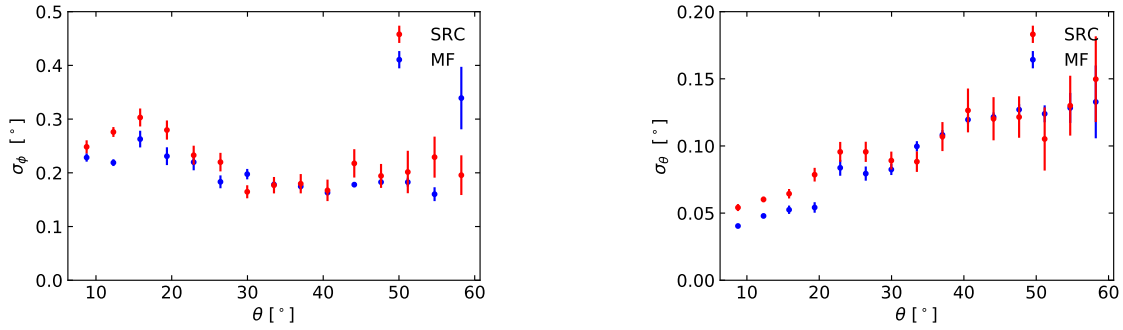

Figure 14: Proton angular resolutions for ϕ (left) and θ (right) for this study.

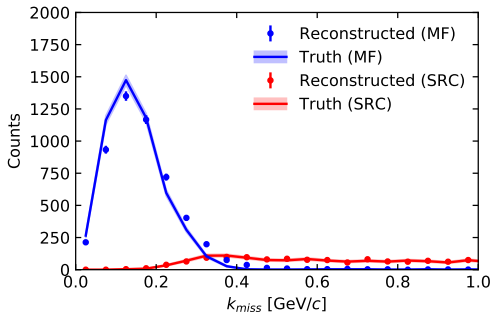

Figure 15: Distributions of k_{miss} for mean-field (blue) and SRC (red) events, including the effects of bin migration.

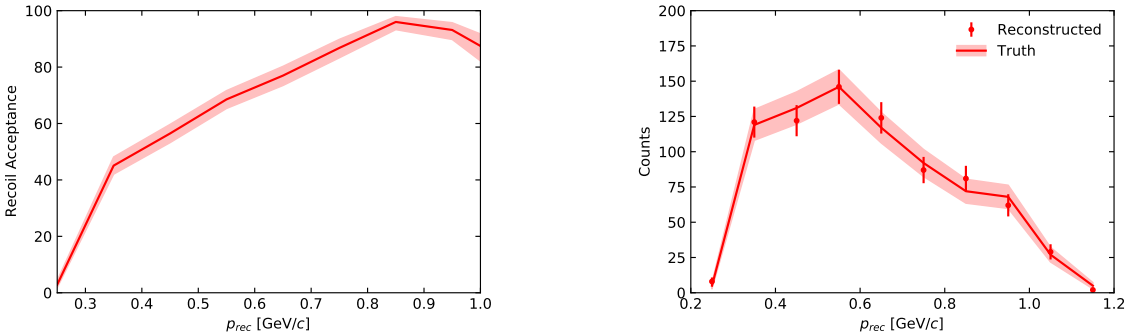

Figure 16: Recoil proton detection rate (left) and momentum distribution (right), including the effects of bin migration.

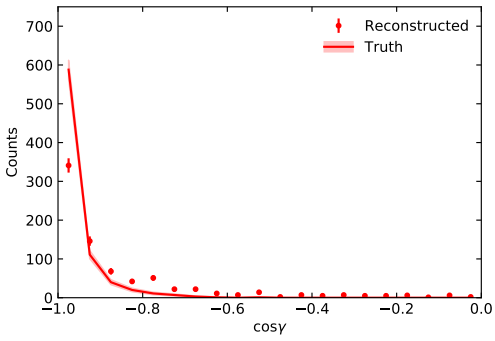

Figure 17: Distribution of the opening angle between the missing momentum and the detected recoil proton, including the effects of bin migration.

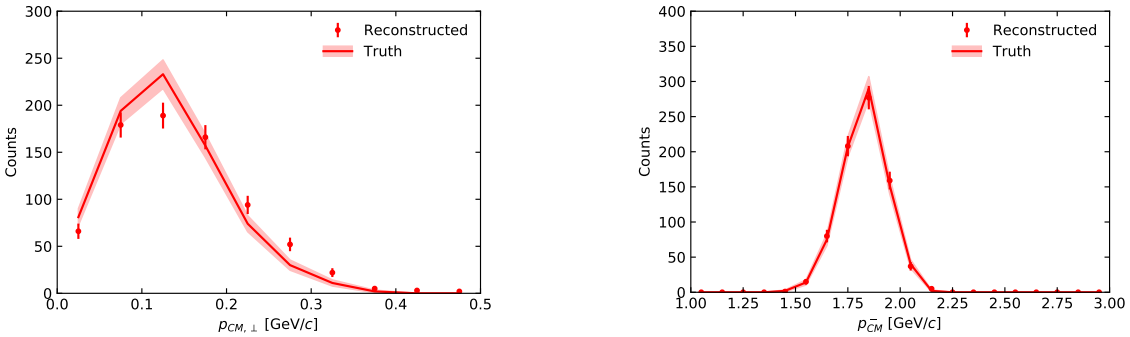

Figure 18: Distributions of $|\mathbf{p_{CM,\perp}}|$ (left) and p^{-}_{CM} (right) for SRC events, including the effects of bin migration.